Concurrent Real-Time Estimation of State of Health and Maximum Available Power in Lithium-Sulfur Batteries

Authors:

Vaclav Knap, Daniel J. Auger, Karsten Propp, Abbas Fotouhi, Daniel-Ioan Stroe

Abstract:

Lithium-sulfur (Li-S) batteries are an emerging energy storage technology with higher performance than lithium-ion batteries in terms of specific capacity and energy density. However, several scientific and technological gaps need to be filled before Li-S batteries will penetrate the market at a large scale. One such gap, which is tackled in this paper, is represented by the estimation of state-of-health (SOH). Li-S batteries exhibit a complex behaviour due to their inherent mechanisms, which requires a special tailoring of the already literature-available state-of-charge (SOC) and SOH estimation algorithms. In this work, a model of SOH based on capacity fade and power fade has been proposed and incorporated in a state estimator using dual extended Kalman filters has been used to simultaneously estimate Li-S SOC and SOH. The dual extended Kalman filter's internal estimates of equivalent circuit network parameters have also been used to the estimate maximum available power of the battery at any specified instant. The proposed estimators have been successfully applied to both fresh and aged Li-S pouch cells, showing that they can accurately track accurately the battery SOC, SOH, and power, providing that initial conditions are suitable. However, the estimation of the Li-S battery cells' capacity fade is shown to be more complex, because the practical available capacity varies highly with the applied current rates and the dynamics of the mission profile.

Concurrent Real-Time Estimation of State of Health and Maximum Available Power in Lithium-Sulfur Batteries

Vaclav Knap [1,*] 🆔 **, Daniel J. Auger** [2] 🆔 **, Karsten Propp** [2] **, Abbas Fotouhi** [2] 🆔 **and Daniel-Ioan Stroe** [1] 🆔

[1] Department of Energy, Aalborg University, 9220 Aalborg, Denmark; dis@et.aau.dk
[2] School of Aerospace, Transport and Manufacturing, Cranfield University, College Road, Cranfield, Bedford MK43 0AL, UK; d.j.auger@cranfield.ac.uk (D.J.A.); k.propp@cranfield.ac.uk (K.P.); a.fotouhi@cranfield.ac.uk (A.F.)
* Correspondence: vkn@et.aau.dk

Abstract: Lithium-sulfur (Li-S) batteries are an emerging energy storage technology with higher performance than lithium-ion batteries in terms of specific capacity and energy density. However, several scientific and technological gaps need to be filled before Li-S batteries will penetrate the market at a large scale. One such gap, which is tackled in this paper, is represented by the estimation of state-of-health (SOH). Li-S batteries exhibit a complex behaviour due to their inherent mechanisms, which requires a special tailoring of the already literature-available state-of-charge (SOC) and SOH estimation algorithms. In this work, a model of SOH based on capacity fade and power fade has been proposed and incorporated in a state estimator using dual extended Kalman filters has been used to simultaneously estimate Li-S SOC and SOH. The dual extended Kalman filter's internal estimates of equivalent circuit network parameters have also been used to the estimate maximum available power of the battery at any specified instant. The proposed estimators have been successfully applied to both fresh and aged Li-S pouch cells, showing that they can accurately track accurately the battery SOC, SOH, and power, providing that initial conditions are suitable. However, the estimation of the Li-S battery cells' capacity fade is shown to be more complex, because the practical available capacity varies highly with the applied current rates and the dynamics of the mission profile.

Keywords: extended Kalman filter; Lithium-Sulfur battery; maximum available power; state of charge; state of health

1. Introduction

Growing demands from original equipment manufacturers (OEMs) and users for lighter batteries with a higher capacity has lead to research into and development of new energy storage technologies such as Lithium-Sulfur (Li-S) batteries. This technology represents a suitable alternative to nowadays broadly used Lithium-ion (li-ion) battery cells as they are characterized by six times higher theoretical specific energy and two times higher theoretical energy density than traditional Li-ion batteries [1]. Furthermore, Li-S batteries are expected to be cheaper, as they use sulfur as a raw material, [1] and safer [2]. However, there are still obstacles to their successful large-scale commercialization. The first type of obstacles is related to the actual cell performance and lifetime, which are hindered problems such as the fast capacity fade during cycling [3] and the high self-discharge at high state-of-charge (SOC) levels [4]. While the chemical challenges are addressed at cell development or material level [5], there are also practical challenges that have to be addressed by system design, in order to operate the Li-S cells in a safe and optimal way due to their complex chemistry [6].

1.1. State-of-Charge and State-of-Health Estimation

The battery management system (BMS) is vital in the practical use of batteries, as it takes care of the safe and efficient operation of the battery [7]. Typically, advanced BMSs include state estimation functions, which provide information about state-of-charge (SOC) and state-of-health (SOH), which are crucial for effective and reliable battery function and also useful to the user.

Many different methods for the state estimation have been proposed in the literature. Frequently-mentioned methods for SOC estimation are: ampere-hour counting, open-circuit voltage (OCV) based, model based, impedance based, static battery characteristics based, fuzzy logic and machine learning based estimations [8]. Each of these methods has its advantages and drawbacks, which makes them suitable for different battery technologies. SOH estimation is usually based on various capacity and/or impedance estimation techniques and also correlations of those quantities to some observable effects [7]. These estimation techniques are usually tailored to specific battery chemistries, as they might have unique attributes and behaviour. It is possible to find many works which have been done on widely used Lead-acid [9–11], Nickel-metal Hydride (NiMH) [12–14] and Lithium-ion [11,15,16] batteries. However, these methods, successfully applied to other battery chemistries, are not directly applicable for Li-S batteries, due to the particularities of this technology. For example, the Coulomb counting method is not suitable due to the high self-discharge [4] and due to the variable shape and length of voltage charging curve, which is caused by the polysulfide shuttle and 'history' effect [17]. Moreover, the Li-S batteries have a unique shape of the open-circuit voltage [18], which is flat for the interval 0 to 70% SOC. Furthermore, a voltage 'dip' occurs during discharging between the high and the low voltage plateaus, which causes non-monotonic voltage trend. This reduces their observability and it prevents the use of any open-circuit voltage based technique.

To the present day, in the field of Li-S batteries, there has been proposed and demonstrated only a limited number of functional approaches to SOC estimation. A technique based on Kalman variant estimators (extended Kalman filter (EKF), unscented filter and particle filter) was presented in reference [19]; in that work, the filter was applied to the battery model, developed in reference [20], in a classical manner, meaning that the SOC was estimated according to a combination of Coulomb counting and voltage response of the battery. The SOC was estimated with a root square mean error (RSME) of 0.0114 for mixed pulse discharge profile scenario and 0.0217 RSME for New European Driving Cycle (NEDC) driving profile for the correct initial state. In a scenario, when the initial SOC was lower than the actual battery state (0.7 instead of 1), the estimated SOC by EKF converged quickly towards the reference state. However, when the initial SOC was set lower (i.e., 0.6), the estimated state did not converge over one full discharge. Moreover, when the estimation was applied to partially charged cell (initial reference SOC was 0.6), the estimator showed a poor accuracy and in the case of initial estimator SOC being set to 1, it also did not converge over one full discharge. Another approach for state estimation of Li-S batteries, discussed in reference [18], is based on the observability of the SOC from the battery parameters, such as open-circuit voltage and internal resistance. This method can provide advantages as these identified parameters might be easier to track and express during the laboratory degradation tests than the complex battery voltage response used in previously mentioned approach. The first step, following this approach, is to implement an online battery parameter identification algorithm. Three identification algorithms: gradient descent, genetic algorithm and prediction error minimization were investigated and compared in reference [21], where also the SOC estimation of a NiMH battery based on an adaptive neuro-fuzzy inference system (ANFIS) was demonstrated, which can be in a similar way applied to the Li-S battery. Furthermore, the parameter identification can be also based on the extended Kalman filter, which was presented for Li-S batteries in reference [22], and it was directly used in a dual Kalman filter manner for the SOC estimation of Li-S batteries. Accordingly, we can summarize that there exists already some base ground for the SOC estimation at Li-S batteries. Nevertheless, the robustness of estimation needs to be improved, especially in cases when the initially set SOC does not match the actual battery SOC,

then the convergence has to be ensured. Moreover, the estimation needs to be validated not only at the fresh cell, but also at an aged cell, as battery parameters change during aging.

The area of SOH estimation for Li-S batteries has not been covered at all. Therefore, in this paper we introduce a combined SOC and SOH estimation algorithm, which is based on the parameter identification method introduced by Propp et al. [22]. The proposed SOH estimation method allows to estimate the capacity fade and resistance change caused by the battery aging without the use of any degradation model, which is especially beneficial at the current stage of reduced knowledge and practical experience with the Li-S batteries.

1.2. Maximum Available Power Estimation

Besides the SOC and SOH estimation, another function required of the BMS is estimation of the available power. Especially in electric vehicle applications, there are certain situations when the high power is required from the battery, for example during the acceleration. In these situations, the safety operation limits can be reached quickly, which will result into limitation of the provided power and its sudden decrease, causing an unexpected and possibly dangerous situation for a driver. Therefore, the estimation of the available power is applied to predict the maximum power which can be provided, typically in period of 1 to 20 seconds. In this way, the provided power can be limited from the beginning, causing the smooth operation and expected continuous decrease later on [7].

There are usually considered to be three main methods for the estimation of the available power. The first is based on a characteristic map, which is stored in a memory of the BMS. It is composed of static relationships of power towards the other battery states and quantities and it is obtained offline from the battery tests. During aging, some of the battery parameter changes, and thus the characteristic map has to be updated. The advantage of this method is its easy implementation and simplicity. However, it does not reflect the dynamic states of the battery accurately and it might be difficult to adjust it during the aging due to lack of the reference measurements (at maximum power). Moreover, it might required considerable space of the memory to store all the data with the inter-dependencies [7,23].

The second method is based on a dynamic battery model. The maximum power is then predicted according the accuracy of the battery model, reflecting the dynamic states. The obvious advantage of this method in our context is that the battery parameters can be identified online. Therefore, the battery parameters would be adjusted according to aging and also specific chemistry effects (a history effect of the Li-S batteries) to provide more precise estimated [7,24].

The third method, considered for this purpose, uses ANFIS. However, an additional filtering is required for training on power pulses. Moreover, the real-time applicability on a low cost hardware is questionable [7,25].

To the authors' best knowledge, there are no examples of maximum available power estimator for Li-S batteries in the literature. Thus we target this area in this work and present such estimator.

This paper is structured as follows. The methodology for modelling and state estimation is described in Section 2. This includes definitions of battery states in terms of state of charge, health and maximum available power; and a description of the considered Li-S battery model. The section introduces a standard implementation of an Extended Kalman filter, an online parameter identification method, a maximum available power estimation approach and a metric for an estimation evaluation. The specific implementation of the SOC and SOH estimation algorithms is presented in Section 3. The results for SOC, SOH and maximum available power estimation are described and shown in Section 4. The paper is concluded in Section 5.

2. Methodology

2.1. State Definitions

States of the battery receive a great amount of an interest. However, they are not always perceived in the same and unique way. There is more consensus about the state-of-charge definition, which is usually understood as an amount of charge, which is available to be extracted from the actual battery capacity [7,26]. Sometimes, the nominal capacity term is used instead of the actual capacity [27]. However, that might lead to an incorrect assumption of neglecting the capacity change during the battery life. Moreover, the amount of the extractable charge in the battery varies with the temperature or the applied current. The capacity dependence of the current is typically described by Peukert's law [28]. Extending the Peukert equation by a temperature dependency was described in [29].

As an indicator for the state of health of the battery, the most commonly used is a change in the actual capacity, a capacity fade [10,13]. Some methods estimate the capacity fade according to its relationship to the change of impedance, which is usually growing during the battery aging [30]. Furthermore, the impedance was accommodated as an another indicator for the SOH [15,26] and it is also related to the maximum available power of the battery, as the impedance growth contributes a lot to the power fade. However, other factors might also be considered for the SOH estimation [27], as for example the porosity of the electrodes [31] or the terminal voltage [32].

The maximum available power is the power actually achievable from the battery with respect to its safety limits and internal and external conditions [7].

To summarize, it is important to clearly state which definition is followed in the work. Definitions in this work are based on [7,26], where the initial capacity $\bar{Q}_{\text{cap}}$ is the maximum extractable charge from the fully charged battery at the beginning of life under the specific conditions (i.e., temperature, C-rate, cut-off limits). The actual capacity Q_{cap} represents the maximum extractable charge from the fully charged battery at the actual battery age under the specific conditions. The definitions for the initial internal resistance $\bar{R}_0$ and the actual internal resistance R_0 correspond to similar definitions to the capacity definitions, but to the internal resistance instead of the capacity.

State-of-charge: SOC represents a present amount of charge Q_{present}, which is possible to extract from the battery, related to the actual capacity. It is noted as χ and expressed as:

$$\text{SOC} = \chi = \frac{Q_{\text{present}}}{Q_{\text{cap}}}. \tag{1}$$

State of health: SOH consists of two quantities representing capacity fade η_{Q} and internal resistance change η_{R}. The SOH can be written as:

$$\text{SOH} = [\eta_{\text{Q}} \ \eta_{\text{R}}]^T. \tag{2}$$

The capacity fade (η_{Q}) is computed as the actual capacity divided by the nominal capacity at the beginning of life:

$$\eta_{\text{Q}} = \frac{Q_{\text{cap}}}{\bar{Q}_{\text{cap}}}. \tag{3}$$

The internal resistance change (η_{R}) is computed as the internal resistance at the beginning of life divided by the actual internal resistance:

$$\eta_{\text{R}} = \frac{\bar{R}_0}{R_0}. \tag{4}$$

Maximum available power: $P_{\text{dis.max}} / P_{\text{ch.max}}$ is considered in this work to be limited only by current and voltage limits. Generally, it can be written as:

$$P_{\max} = IV, \tag{5}$$

where both current *I* and voltage *V* are limited to not exceed their own safety limits.

2.2. Li-S Battery Model and Its Parametrization

For the estimation of defined states, it is necessary to relate the behaviour of the Li-S cells to them. For the relationship of parameters over the SOC, the Thevenin electrical circuit network, illustrated in Figure 1a, and its behavioural representation, illustrated in Figure 1b, were applied. The details of the derivation of this model are presented in our previous work [20]. In this paper, we introduce the model briefly as the algebra of the following sections rely on it. Tests were based on discharging OXIS Energy 3.4 Ah long life Li-S cells in different temperatures with varying current rates shown in Figure 1c. The original idea of the application of different current pulses was to capture the open-circuit voltage (V_{OC}), the internal resistance (R_0) and the transient behaviour of the cell (R_1, C_1) over its discharge range in addition to exploring the effects of the current rate.
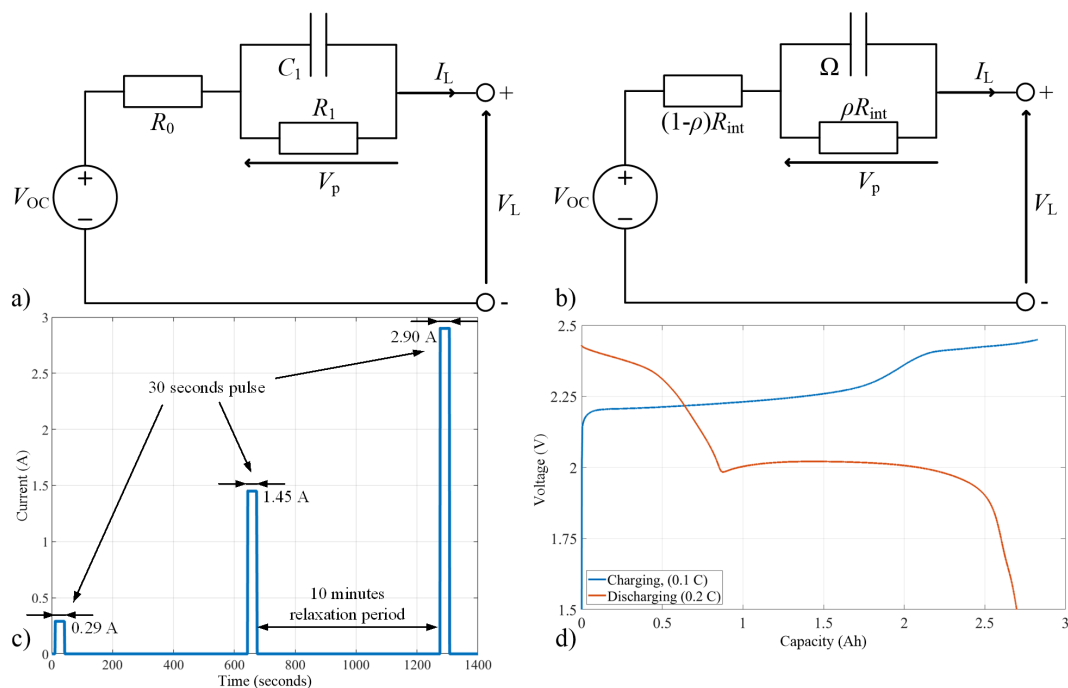

Figure 1. (**a**) Thevenin equivalent circuit model used for modelling the Li-S battery, (**b**) behavioural equivalent circuit model used for modelling the Li-S battery, (**c**) mixed pulse discharge test—the detail on three current pulses, (**d**) a typical continuous charging/discharging profile for a Li-S cell (measured at 25 °C).

However, it was found that the rate dependencies of the model parameters are small and that they could be neglected without decreasing the model accuracy significantly. Since the model's intentional usage is also the state estimation, polynomial functions in the form of

$$f_{parameter}(\chi) = p_{10}x_1^9 + p_9x_1^8 + p_8x_1^7 + p_7x_1^6 + p_6x_1^5 + p_5x_1^4 + p_4x_1^3 + p_3x_1^2 + p_2x_1 + p_1 \tag{6}$$

were fitted describing the parameters over the SOC. While fitted polynomial functions are generally a standard method, it is difficult to reproduce the harsh transitions between the high- and low-plateau of the Li-S cells with them. Therefore, two polynomial functions were combined for the V_{OC} and R_0 and joined together at the transition point. The model implements combined functions for the V_{OC}

$$f_{V_{\text{OC}}}(\chi) = (1 - \gamma_{\text{m,c}}(\chi))\ f_{V_{\text{OC}}-\text{low}}(\chi)$$
$$+\gamma_{\text{m,c}}(\chi)\ f_{V_{\text{OC}}-\text{high}}(\chi) \tag{7}$$

and R_0

$$f_{R_0}(\chi) = (1 - \gamma_{\text{m,c}}(\chi))\ f_{R_0-\text{low}(\chi)}$$
$$+\gamma_{\text{m,c}}(\chi)\ f_{R_0-\text{high}}(\chi). \tag{8}$$

Since the linearisation of the applied Kalman filter methods need differentiable functions, γ combines both polynomials smoothly

$$\gamma_{\text{m,c}}(\chi) := \begin{cases} 0, & \text{if a,} \\ \frac{1}{2} + \frac{1}{2}\sin\left(2m(\chi - c)\right), & \text{if b,} \\ 1, & \text{if c,} \end{cases} \tag{9}$$

where the conditions a, b and c stands for the different ranges of the function:

$$\text{a}:\ 2m(\chi - c) < -\frac{1}{2}\pi,$$
$$\text{b}:\ -\frac{1}{2}\pi \leq 2m(\chi - c) < \frac{1}{2}\pi, \tag{10}$$
$$\text{c}:\ 2m(\chi - c) > \frac{1}{2}\pi,$$

where m is a scaling factor for the maximal gradient of the sinusoidal function, determining the transition range between both polynomials and c represents the point where both functions are equally represented. The resulting state space model has the form

$$\dot{x}(t) = A(t)x(t) + B(t)u(t),$$
$$y(t) = C(t)x(t) + D(t)u(t), \tag{11}$$

which relies on the nonlinear functions of $V_{\text{OC}}, R_0, C_1, R_1$ over the SOC. The dynamic states $x = [x_1\ x_2]^T$ of the system are the voltage over the RC circuit V_{p} and the SOC χ, calculated through Coulomb counting. The corresponding state space representation gives

$$A = \begin{bmatrix} \frac{-1}{f_{R_1}(\chi)\,f_{C_1}(\chi)} & 0 \\ 0 & 0 \end{bmatrix} \quad B = \begin{bmatrix} \frac{1}{f_{C_1}(\chi)} \\ \frac{-1}{3600Q_{\text{cap}}} \end{bmatrix}$$
$$C = \begin{bmatrix} -1 & f_{V_{\text{OC}}}(\chi) \end{bmatrix} \quad D = \begin{bmatrix} f_{R_0}(\chi) \end{bmatrix}. \tag{12}$$

Alternatively, the core Thevenin battery model equations are written as:

$$V_{\text{L}} = V_{\text{OC}}(\chi) - R_0(\chi)I_{\text{L}} - V_{\text{p}}, \tag{13}$$
$$\frac{dV_{\text{p}}}{dt} = -\frac{1}{R_1(\chi)C_1(\chi)}V_{\text{p}} + \frac{1}{C_1(\chi)}I_{\text{L}}. \tag{14}$$

The behavioural battery model representations, described in [20], introduces parameters representing the dynamic bandwidth (Ω), the total steady-state resistance (R_{int}) and the dynamic fraction of the response (ρ), instead of R_0, R_1 and C_1. The parameters inter-relations are defined as:

$$\Omega(\chi) = \frac{1}{R_1(\chi)C_1(\chi)}, \tag{15}$$

$$R_{\text{int}}(\chi) = R_0(\chi) + R_1(\chi),\tag{16}$$

$$\rho(\chi) = \frac{R_1(\chi)}{R_{\text{int}}(\chi)}.\tag{17}$$

By substituting Equations (15), (16) and (17) into Equations (13) and (14), the following behavioural model equations are obtained:

$$V_{\text{L}} = V_{\text{OC}}(\chi) - (1 - \rho(\chi))R_{\text{int}}(\chi)I_{\text{L}} - V_{\text{p}},\tag{18}$$

$$\frac{dV_{\text{p}}}{dt} = -\Omega(\chi)V_{\text{p}} + \rho(\chi)R_{\text{int}}(\chi)\Omega(\chi)I_{\text{L}}.\tag{19}$$

2.3. Standard Extended Kalman Filter Implementation

The EKF implementation described in detail can be found for example in [33,34]. The EKF consists of two steps: time update and measurement update. During the time update, the state is estimated ahead in time (predicted) and, during the measurement update, the state is adjusted (corrected) according an actual measurement at that time. The representation of the EKF update equations with approximation of the state and measurement vector without noise values can be written as:

Time update (prediction):

$$x_k^- = f(x_{k-1}, u_{k-1}, 0),\tag{20}$$

$$P_k^- = A_k P_{k-1} A_k^T + Q_{k-1},\tag{21}$$

$$y_k^- = h(x_k^-, 0),\tag{22}$$

Measurement update (correction):

$$K_k = P_k^- C_{k-1}^T (C_k P_k^- C_k^T + R_{k-1})^{-1},\tag{23}$$

$$x_k = x_k^- + K_k(y_k - y_k^-),\tag{24}$$

$$P_k = (I - K_k C_k)P_k^-.\tag{25}$$

The process and noise measurement covariance matrices are formed as

$$Q_k = E[w_k w_k^T], R_k = E[v_k v_k^T].\tag{26}$$

2.4. Online Parameter Identification

In contrast to the standard state estimation, where a model identified offline is used to predict the system's output and the error between the prediction and measurements is used to correct the states of interest, an online parameter identification method can be used to identify the parameters directly. However, this means that the identification has to be fast enough to run on common BMS hardware and that the identification results have to be reliable with different current profiles. While the main concept of online identification was proposed in [35–37] for common Li-ion batteries, Propp et al. [22] adapted the identification for Li-S batteries. Since the principles of this work are used here as well, they are also introduced here briefly. The online parametrization fits the parameters with the derivative of the terminal battery voltage V_{L} of the Thevenin model

$$\dot{V}_{\text{L}} = \dot{V}_{\text{OC}} - \dot{V}_{\text{p}} - \dot{I}_{\text{L}} R_0 - I_{\text{L}} \dot{R}_0.\tag{27}$$

Generally, the OCV of the battery is dependent on the SOC, the operating temperature (T) and usage history (h). Therefore, the corresponding definition of V_{OC} can be described as a function of SOC, T, h, whose derivation leads to

$$\dot{V}_{OC} = \frac{\delta V_{OC}}{\delta SOC}\frac{\delta SOC}{\delta t} + \frac{\delta V_{OC}}{\delta T}\frac{\delta T}{\delta t} + \frac{\delta V_{OC}}{\delta h}\frac{\delta h}{\delta t}. \tag{28}$$

For the representation of the battery in a discrete manner, usually time steps of less than one second are used. Slow changing parameters therefore can be eliminated from the equation for simplification. Thus, the SOC $\left(\frac{\delta SOC}{\delta t} \approx 0\right)$, the change of the OCV over time $\left(\frac{\delta V_{OC}}{\delta t} \approx 0\right)$, the temperature changes $\left(\frac{\delta T}{\delta t} \approx 0\right)$ and the long-term history $\left(\frac{\delta h}{\delta t} \approx 0\right)$ can be approximated as 0. It is furthermore assumed that the internal resistance variation are negligible ($\dot{R}_0 \approx 0$) for small periods. The resulting simplified relationship for the terminal voltage over time

$$\dot{V}_L = -\dot{V}_p - R_0\dot{I}_L \tag{29}$$

was then changed to a behavioural interpretation to improve the identification process. For the terminal voltage,

$$\dot{V}_L = -\dot{V}_p - (1-\rho)R_{int}\dot{I}_L, \tag{30}$$

and for the voltage drop over the RC circuit,

$$\dot{V}_p = -\Omega\, V_p + \rho\, R_{int}\, \Omega\, I_L. \tag{31}$$

By re-writing the behavioural interpretation of the equation for the terminal battery voltage

$$V_L = V_{OC} - V_p - \underbrace{(1-\rho)R_{int}}_{\text{formally } R_0}\, I_L \tag{32}$$

to bring V_p on one side, substituting it into Equation (31) and including the result for $\dot{V}_p$ in Equation (30), the behavioural state transition equation can be derived as

$$\dot{V}_L = \Omega\big(V_{OC} - V_L - (1-\rho)R_{int}I_L\big) - \rho\, R_{int}\, \Omega\, I_L - (1-\rho)R_{int}\dot{I}_L. \tag{33}$$

For the online identification with a Kalman filter based algorithm, the system is now expressed by its parameters as the state vector

$$x = \begin{bmatrix} V_{OC} & V_L & V_p & \Omega & \rho & R_{int} \end{bmatrix}^T. \tag{34}$$

With the corresponding state transition functions from Equations (31) and (33), the input current $I_L = u$ and the previous considerations the state transition functions can be populated as

$$f(x,u) = \begin{bmatrix} f_1 & f_2 & f_3 & f_4 & f_5 & f_6 \end{bmatrix}^T, \tag{35}$$

where f_1 to f_6 are defined as:

$$f_1 = 0,\ f_4 = 0,\ f_5 = 0,\ f_6 = 0, \tag{36}$$

$$f_2 = x_1 x_4 - x_2 x_4 - x_4(1-x_5)x_6 u - x_6 - x_5 x_6 x_4 u - (1-x_5)x_6\dot{u}, \tag{37}$$

$$f_3 = -x_4 x_3 + x_5 x_6 x_4 u. \tag{38}$$

Since the measured terminal voltage of the battery is represented by the second state, the measurement equation is

$$h = x_2. \tag{39}$$

The Jacobians for the presented functions f_1 to f_6, linearising the system around the current mean for the extended Kalman filter, are therefore:

$$A = \begin{bmatrix} 0 & 0 & 0 & 0 & 0 & 0 \\ x_4 & -x_4 & 0 & x_1 - x_2 - x_6 u & x_6 \dot{u} & a_{2,6} \\ 0 & 0 & -x_4 & -x_3 + x_5 x_6 u & x_6 x_4 u & x_5 x_4 u \\ 0 & 0 & 0 & 0 & 0 & 0 \\ 0 & 0 & 0 & 0 & 0 & 0 \\ 0 & 0 & 0 & 0 & 0 & 0 \end{bmatrix}, \tag{40}$$

$$a_{2,6} = -x_4 u - \dot{u} + x_5 \dot{u}.$$

C can be obtained as

$$C = \begin{bmatrix} 0 & 1 & 0 & 0 & 0 & 0 \end{bmatrix}. \tag{41}$$

This method has been proven to show robust identification results as long as there are some dynamics in the current profile. To apply the introduced online parametrization, the system has to be implemented in an extended Kalman filter algorithm, which is introduced in the following section.

2.5. Structure of the Maximum Available Power Estimation

The implemented maximum available power estimation is based on the dynamic battery model approach, when the battery parameters are identified online. The estimation is derived accordingly:

The Laplace transform of equation (19) is

$$s\bar{V}_P - V_{p0} = -s\Omega\bar{V}_P + \rho R_{int}\Omega\bar{i}_L, \tag{42}$$

which can be rearranged as

$$(s + \Omega)\bar{V}_P = \rho R_{int}\Omega\bar{i}_L + V_{p0} \tag{43}$$

and again to

$$\bar{V}_P = \underbrace{\rho R_{int} \cdot \frac{\Omega}{s + \Omega}}_{\text{transfer function}} \cdot \bar{i}_L + \underbrace{\left(\frac{V_{p0}}{\Omega}\right)\frac{\Omega}{s + \Omega}}_{\text{initial condition}}. \tag{44}$$

Let us assume that the future current has a constant value, I_L. Note that

$$\mathcal{L}\{I_L\} = \frac{I_L}{s}. \tag{45}$$

Substituting this in equations (18) and (44) gives

$$V_L = V_{OC} - (1 - \rho)R_{int}I_L - V_p, \tag{46}$$

$$\bar{V}_P = \rho R_{int}I_L \cdot \frac{\Omega}{s(s + \Omega)} + V_{p0} \cdot \frac{1}{s + \Omega}. \tag{47}$$

Now,

$$\frac{\Omega}{s(s + \Omega)} = \frac{1}{s} - \frac{1}{s + \Omega} \tag{48}$$

so

$$\bar{V}_P = \rho R_{int}I_L \cdot \frac{1}{s} + \left(V_{p0} - \rho R_{int}I_L\right)\frac{1}{s + \Omega}. \tag{49}$$

We can take the inverse Laplace transform:

$$V_{\mathrm{p}}(t) = \rho R_{\mathrm{int}} I_{\mathrm{L}} + (V_{\mathrm{p0}} - \rho R_{\mathrm{int}} I_{\mathrm{L}}) e^{-\Omega t} \tag{50}$$

so we end up with

$$V_{\mathrm{L}}(t) = V_{\mathrm{OC}} - R_{\mathrm{int}} I_{\mathrm{L}} + (\rho R_{\mathrm{int}} I_{\mathrm{L}} - V_{\mathrm{p0}}) e^{-\Omega t} \tag{51}$$

or, equivalently,

$$V_{\mathrm{L}}(t) = (V_{\mathrm{OC}} - V_{\mathrm{p0}} e^{-\Omega t}) - R_{\mathrm{int}} (1 - \rho \cdot e^{-\Omega t}) I_{\mathrm{L}}. \tag{52}$$

Let us assume that at some point $T \geq 0$ seconds in the future, we want to know the minimum and maximum currents such that $V_{\mathrm{L}}(T) \in [V_{\mathrm{min}}, V_{\mathrm{max}}]$. For convenience, we can write

$$V' = V_{\mathrm{OC}} - V_{\mathrm{p0}} e^{-\Omega T} \tag{53}$$

and

$$R' = R_{\mathrm{int}} (1 - \rho e^{-\Omega T}). \tag{54}$$

In practical applications, $V', R' > 0$ since $V_{\mathrm{OC}} > V_{\mathrm{p0}}$ and $\rho < 1$. We can then write

$$V_{\mathrm{L}}(T) = V' - R' I_{\mathrm{L}}. \tag{55}$$

To keep $V_{\mathrm{L}}(T) \in [V_{\mathrm{min}}, V_{\mathrm{max}}]$, we need to satisfy

$$V_{\mathrm{min}} \leq V' - R' I_{\mathrm{L}}, \tag{56}$$

which becomes

$$I_{\mathrm{L}} \leq I_{V_{\mathrm{min}}}, \tag{57}$$

where $I_{V_{\mathrm{min}}} = (V' - V_{\mathrm{min}})/R'$; similarly, we need

$$V_{\mathrm{max}} \geq V' - R' I_{\mathrm{L}}, \tag{58}$$

which becomes

$$I_{\mathrm{L}} \geq I_{V_{\mathrm{max}}}, \tag{59}$$

where

$$I_{V_{\mathrm{max}}} = -(V_{\mathrm{max}} - V')/R'. \tag{60}$$

In practice, we are likely to also want to ensure that the current is constrained to a specified window, $I_{\mathrm{L}} \in [I_{\mathrm{min}}, I_{\mathrm{max}}]$. The most conservative of these will be the most important. Effectively, the current that gives the maximum discharge power is given by

$$I_{P_{\mathrm{dis.max}}} = \min\left(I_{V_{\mathrm{min}}}, I_{\mathrm{max}}\right), \tag{61}$$

with the corresponding power given by

$$P_{\mathrm{dis.max}} = \left(V' - R' I_{P_{\mathrm{dis.max}}}\right) I_{P_{\mathrm{dis.max}}}. \tag{62}$$

Similarly, the current that gives the maximum charge power is

$$I_{P_{\mathrm{ch.max}}} = \max\left(I_{V_{\mathrm{max}}}, I_{\mathrm{min}}\right), \tag{63}$$

with the corresponding power given by

$$P_{\text{ch.max}} = \left(V' - R' I_{P_{\text{ch.max}}} \right) I_{P_{\text{ch.max}}}. \tag{64}$$

2.6. Estimation Evaluation

The estimation algorithms are evaluated according their absolute maximum error:

$$x_{\_\text{MaxErr}} = \begin{bmatrix} \max(|\chi_{\_\text{Ref}} - \chi_{\_\text{Est}}|) \\ \max(|\eta_{\text{Q}\_\text{Ref}} - \eta_{\text{Q}\_\text{Est}}|) \\ \max(|\eta_{\text{R}\_\text{Ref}} - \eta_{\text{R}\_\text{Est}}|) \end{bmatrix} \tag{65}$$

and their absolute mean error:

$$x_{\_\text{AvgErr}} = \begin{bmatrix} \frac{1}{n} \sum_{t=1}^{n} (|\chi_{\_\text{Ref}} - \chi_{\_\text{Est}}|) \\ \frac{1}{n} \sum_{t=1}^{n} (|\eta_{\text{Q}\_\text{Ref}} - \eta_{\text{Q}\_\text{Est}}|) \\ \frac{1}{n} \sum_{t=1}^{n} (|\eta_{\text{R}\_\text{Ref}} - \eta_{\text{R}\_\text{Est}}|) \end{bmatrix}. \tag{66}$$

The subscript "Est" stands for estimated states and the subscript "Ref" represents reference values of the states. The reference states are obtained from an offline analysis of the measurements. Coulomb counting provides reference for χ. Moreover, obtained data from the parametrization (Section 2.2) are used as a reference for capacity fade η_{Q} and the resistance change η_{R}.

2.7. Test Procedure and Model Structure

The laboratory tests were performed as the base for tunning and evaluation of the estimators. The current profiles (in this work, specifically considered mixed pulse discharge, NEDC and Urban Dynamometer Driving Schedule (UDDS)) were applied to the battery, which was placed at the thermal chamber with the controlled temperature environment and it was connected to the battery test station. The tests on the fresh cell were done in a MACCOR battery test system (supplied by MACCOR inc.,Tulsa, OK, USA) and the tests on the aged cell were performed in a Digatron battery test system (supplied by Digatron Power Electronics, Aachen, Germany). The measured quantities of the battery, such as current and voltage, were recorded and they were used as an input to the model with the estimators. The temperature for the simulations was considered constant of 20 °C. The layout of the test procedure is in Figure 2.
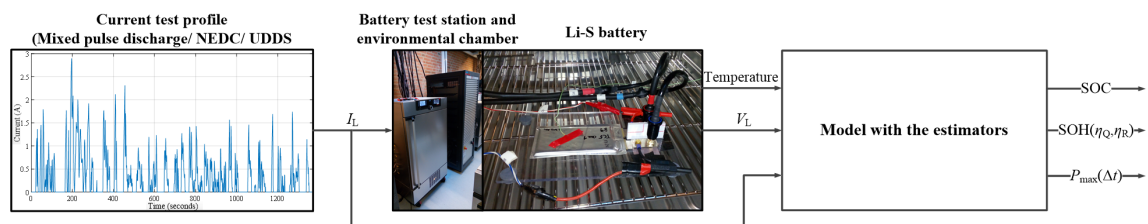

Figure 2. Test procedure layout.

The model layout with the estimators is shown in Figure 3. Current, voltage and temperature are the inputs. The first extended Kalman filter estimates online the circuit model parameters in terms of behaviour model, which are also translated to Thevenin model parameters. The estimated parameters V_{OC} and R_0 are fed, together with current and temperature, into the SOC and SOH estimator, which returns the outputs of χ, η_{Q} and η_{R}. Furthermore, all the behaviour circuit model parameters are used as the input for the maximum available power estimator, which estimates the maximum available power in the specific time period Δt for charging and discharging, together with maximum available current and voltage.
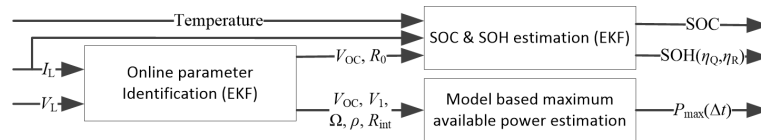
Figure 3. Model layout with the topology of the estimators.

3. Implementation

3.1. Modelling and Structure of the Filters

The states of the interest are SOC (χ) and SOH (η_Q, η_R). Therefore, the state vector is constructed as:

$$x = \begin{bmatrix} \chi \\ \eta_Q \\ \eta_R \end{bmatrix}. \tag{67}$$

The SOC change is based on Coulomb counting. However, no process models for SOH are used, as the change of SOH is assumed to be very slow in comparison to SOC. η_Q and η_R are assumed to be observed from the increasing mean value of the error. The change of state then takes form with consideration of no noise as:

$$\dot{x} = \begin{bmatrix} -\dfrac{I_L}{Q_{cap}*\eta_Q} \\ 0 \\ 0 \end{bmatrix}. \tag{68}$$

The considered measurement vector has form:

$$y = \begin{bmatrix} V_{OC} \\ R_0 \end{bmatrix}, \tag{69}$$

where V_{OC} is open-circuit voltage and R_0 is internal resistance. They are obtained through online parameter identification.

The function $h(x_k^-, 0)$, relating the estimated measurements (estimated parameters V_{OC} and R_0) to the estimated states, is based on the model and the fitted polynomials described in Section 2.2.

The full C matrix for EKF is:

$$C = \begin{bmatrix} \dfrac{\partial V_{OC}}{\partial \chi} & \dfrac{\partial V_{OC}}{\partial \eta_Q} & \dfrac{\partial V_{OC}}{\partial \eta_R} \\ \dfrac{\partial R_0}{\partial \chi} & \dfrac{\partial R_0}{\partial \eta_Q} & \dfrac{\partial R_0}{\partial \eta_R} \end{bmatrix}. \tag{70}$$

With the assumptions that the capacity fade does not have influence on V_{OC} and R_0, together with that resistance change does not influence V_{OC}, the C matrix can be rewritten as:

$$C = \begin{bmatrix} \dfrac{\partial V_{OC}}{\partial \chi} & 0 & 0 \\ \dfrac{\partial R_0}{\partial \chi} & 0 & \dfrac{\partial R_0}{\partial \eta_R} \end{bmatrix} = \begin{bmatrix} c_{11} & 0 & 0 \\ c_{21} & 0 & c_{23} \end{bmatrix}. \tag{71}$$

c_{11} and c_{21} are obtained by the derivative of $h(x_k^-, 0)$ with respect to χ. c_{23} takes the form:

$$c_{23} = \frac{\partial R_0}{\partial \eta_R} = \frac{\partial \frac{\bar{R}_0}{\eta_R}}{\partial \eta_R} = -\frac{\bar{R}_0}{\eta_R^2}. \tag{72}$$

The full A matrix for EKF has the form:

$$A = \begin{bmatrix} \frac{\partial f_\chi}{\partial \chi} & \frac{\partial f_\chi}{\partial \eta_Q} & \frac{\partial f_\chi}{\partial \eta_R} \\ \frac{\partial f_{\eta_Q}}{\partial \chi} & \frac{\partial f_{\eta_Q}}{\partial \eta_Q} & \frac{\partial f_{\eta_Q}}{\partial \eta_R} \\ \frac{\partial f_{\eta_R}}{\partial \chi} & \frac{\partial f_{\eta_R}}{\partial \eta_Q} & \frac{\partial f_{\eta_R}}{\partial \eta_R} \end{bmatrix}, \tag{73}$$

which, without use of any process model for η_Q and η_R, results in:

$$A = \begin{bmatrix} 0 & \frac{\partial f_\chi}{\partial \eta_Q} & 0 \\ 0 & 0 & 0 \\ 0 & 0 & 0 \end{bmatrix} = \begin{bmatrix} 0 & a_{12} & 0 \\ 0 & 0 & 0 \\ 0 & 0 & 0 \end{bmatrix}, \tag{74}$$

$$a_{12} = \frac{\partial f_\chi}{\partial \eta_Q} = \frac{\partial - \frac{I_L}{\bar{Q}_{cap} * \eta_Q}}{\partial \eta_Q} = \frac{I_L}{\eta_Q^2 * \bar{Q}_{cap}}. \tag{75}$$

The observability of such system can be determined from the 'observability grammian' having a full column rank. The grammian takes form as follows in (76), where c_{11} and c_{23} have to be non zero:

$$W_0 = \begin{bmatrix} C \\ CA \\ CA^2 \end{bmatrix} = \begin{bmatrix} c_{11} & 0 & 0 \\ c_{21} & 0 & c_{23} \\ 0 & a_{12} * c_{11} & 0 \\ 0 & a_{12} * c_{21} & 0 \\ 0 & 0 & 0 \\ 0 & 0 & 0 \end{bmatrix}. \tag{76}$$

The linearization of the state change is considered as:

$$\Delta x_k = x_{k-1} + \Delta x * T_s, \tag{77}$$

where T_s is a simulation step size.

3.2. Numerical Values

The initial value for a posteriori error covariance is set as:

$$P = \begin{bmatrix} 0.1 & 0 & 0 \\ 0 & 0.1 & 0 \\ 0 & 0 & 0.1 \end{bmatrix}. \tag{78}$$

The measurement noise covariance R represents a measurement noise of V_{OC} and R_0 and is set to be

$$R = \begin{bmatrix} 0.2^2 & 0 \\ 0 & 0.6^2 \end{bmatrix}, \tag{79}$$

emphasizing higher trusts in the more consistent open circuit voltage identification than the fluctuating internal resistance (Figure 4a). The process noise covariance Q, related to the uncertainty of the process models, is set as:

$$Q = \begin{bmatrix} 0.0001^2 & 0 & 0 \\ 0 & 0.0001^2 & 0 \\ 0 & 0 & 0.1^2 \end{bmatrix}. \tag{80}$$

Here, the arbitrary parameter tuning is based on slow changes, smaller variance values, for the χ and η_Q states and faster parameter changes, or higher variances, for η_R, that need to follow

relatively quick changes at high states of charges (Figure 4c). Furthermore, the states are assumed to be uncorrelated as the diagonal Q matrix indicates.
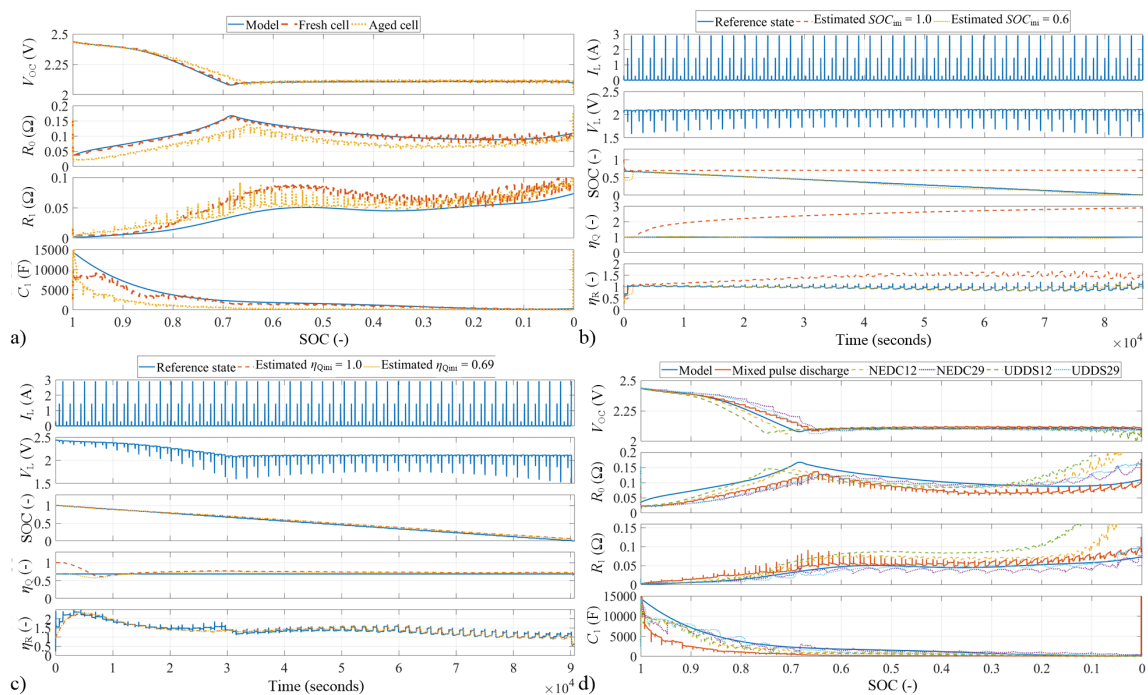

Figure 4. (**a**) comparison of the battery model and online identified parameters for the fresh and aged cell. It shows that, when the cell ages, the inflection point between the high and low voltage plateaus is moving to the right (to lower SOC); (**b**) the mixed pulse discharge test profile and the estimated results for the fresh cell, when the discharge starts already at the low voltage plateau. If the SOC_{ini} is also at the low voltage plateau, the state converges, otherwise they do not; (**c**) the mixed pulse discharge test profile and the estimated results for the aged cell. The estimates converge for all states. The accuracy is higher with the initial estimate closer to the reference state; (**d**) battery model identified parameters for the aged cell at various mission profiles. The absolute available capacity obtained during the discharge causes the shifting of the inflection point at the V_{OC} and R_0 curves due to the SOC relativity to the available capacity. At the end of the discharge, there is a rapid increase of the resistance, dependent on the current rate and the dynamic of the mission profiles.

4. Results

4.1. Fresh Cell—SOC and SOH Estimation

The mixed pulse discharge profile was applied to the fresh cell and the measurement data was fed to the estimator, as illustrated in Figure 2. The reference and estimated states are shown in Figure 5 and their error values are summarized in Table 1. When all the states were initialized with one (= fully charged, fresh cell), the average errors were 0.0080, 0.0125 and 0.0140; and the maximum errors were 0.0306, 0.0559 and 0.7714 for χ, η_Q and η_R, respectively. However, the maximum error value of η_R is caused by the initialization of the parameter estimator and it is reached only at the very beginning. When the current is firstly applied, the resistance quickly converges close to the reference value already after one second. Therefore, the 'real' maximum error of the estimator performance is 0.2606 and the same metric is going to be used further on to evaluate the 'real' performance of the estimator and not the error caused by the parameter estimator initialization. In this ideal case, one can see that the state estimator provides relatively high accurate results with the average error below two percent and the maximum error below six percent. The least reliable state is the η_Q. Moreover, the η_R does not always match the reference, which is probably due to the settling times to reach convergence and also due

to the parameter's dependence on the current. In Figure 4a, one can see that the parameters of V_{OC} and R_0 used for the state estimation are identified very closely to the reference, while the remaining parameters of R_1 and C_1 vary a bit. The R_1 is identified to be slightly higher in the low voltage plateau and the C_1 is identified slightly lower in the high voltage plateau in comparison to the model.

Table 1. The errors of the state estimation for the fresh cell with various initial conditions.

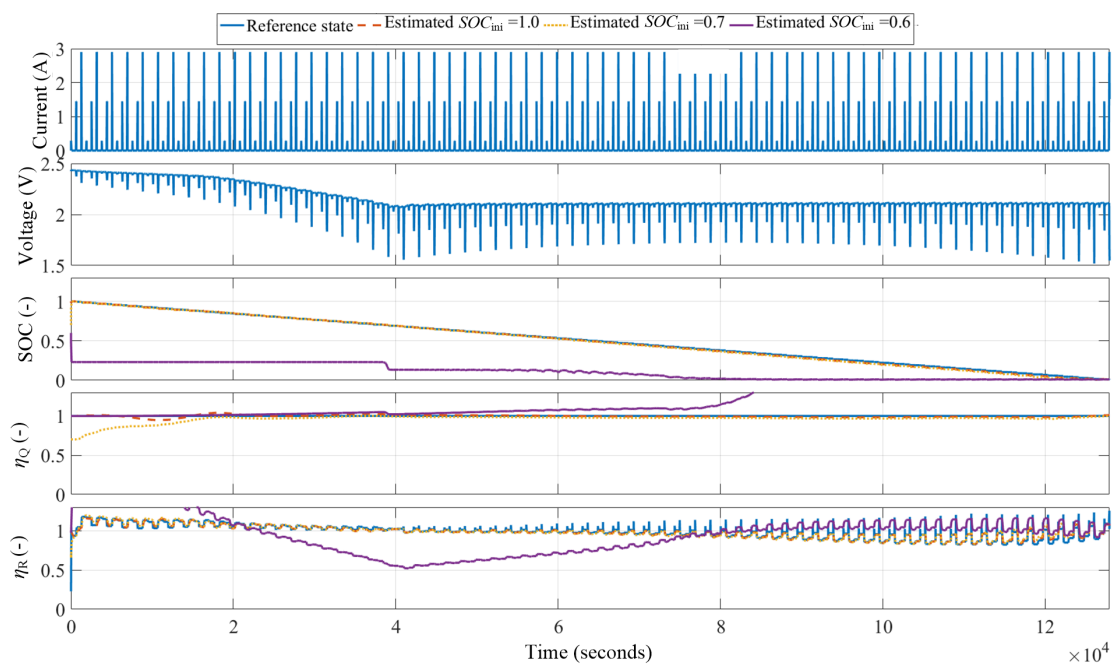| Initial Conditions	Average Errors	Maximum Errors
$[\chi = 1\ \eta_Q = 1\ \eta_R = 1]$	[0.0080 0.0125 0.0140]	[0.0306 0.0559 0.2606]
$[\chi = 0.7\ \eta_Q = 0.7\ \eta_R = 0.7]$	[0.0112 0.0370 0.0174]	[0.1264 0.3000 0.1301]
$[\chi = 0.6\ \eta_Q = 1\ \eta_R = 1]$	[0.3963 0.3796 0.2440]	[0.7688 1.3897 1.2931]

Figure 5. The mixed pulse discharge test profile and the estimated results for the various SOC_{ini} values at the fresh Li-S cell. It shows the capability of the estimator to converge to the states in the cases when the SOC_{ini} is set to match the reference SOC value or to be mismatched, but still on the high voltage plateau as the SOC reference was. If the SOC_{ini} was instead on the low voltage plateau, the estimator was not able to converge.

The next step was to see the convergence capability of the applied Kalman filter when the initial state values are wrongly set. In the first case, all the states are set to be 0.7 in the beginning. From Figure 5, it is apparent that the χ and the η_R converged almost instantly. The χ estimation error was reduced already in the first step of the simulation, after one second, from 0.3 to 0.1264. The error of η_R in the beginning of the simulation was 0.4714, which in 10 seconds of relaxation reduced to 0.4307 and, after the first second of the current being applied, it dropped to 0.1301. The η_Q took a longer amount of time and it continuously settled in the middle of the high voltage plateau, after around 0.15 of SOC is discharged.

So far, the initial SOC (SOC_{ini}) was always set to be on the high voltage plateau. When the SOC_{ini} was set to 0.6, which is on the low voltage plateau, the filter was not able to converge the SOC over the whole discharging period. Moreover, the originally well set η_Q diverged in the second half of the discharge and the η_R was highly off in the first half of the discharge.

To see what happens when the situation is the opposite, the reference SOC is on the low voltage plateau, while the SOC_{ini} is at the high voltage plateau, the simulation was run for only a part of the mixed pulse discharge profile with the initial reference SOC to be 0.6764, which means that the discharge starts already at the low voltage plateau. The obtained results are shown in Figure 4b. When the SOC_{ini} was one, all the states diverged. However, when the SOC_{ini} was 0.6, the states were again estimated very well. Therefore, it is very important that the SOC_{ini} is present at the same voltage plateau as is the reference or real SOC. In the case when the SOC_{ini} was incorrectly set at the high voltage plateau, the η_Q increased rapidly and steadily over the value of 2. Such a 'nonsense' value can be used as an indicator for the incorrect estimation and re-set the estimated SOC value.

This stability issue of the estimator based on the initial conditions of the SOC, whereas the cell is at a high or low voltage plateau can be solved in the following way. The initial conditions for the parameter identification, with a meaning of $[V_{OC}\ V_L\ V_p\ \Omega\ \rho\ R_{int}]$, are adjusted to be:

$$x_0 = \begin{bmatrix} V_{meas} & V_{meas} & 0 & 0.025 & 0.1 & 0.172 \end{bmatrix}^T,$$ (81)

where V_{meas} is the actually measured voltage at the cell. Subsequently, the initialization of the SOC/SOH Kalman filter contains the following condition:

$$SOC_{ini} := \begin{cases} c + 0.01, & \text{if } V_{OC} \geq V_{OC,max\_lp}, \\ c - 0.01, & \text{if } V_{OC} < V_{OC,max\_lp}, \end{cases}$$ (82)

where the c stands for the SOC transition point between the high and low voltage plateau. Moreover, the V_{OC,max_lp} is the maximum V_{OC} value obtained from the Li-S battery model. In such a way, the estimator starts with the SOC_{ini} value, which will lead to the convergence. Of course, if the more accurate guess of the initial condition exists, it shall be inputted.

4.2. Aged Cell—SOC and SOH Estimation

The goal of the SOH estimation is to estimate and track the health of the cell. The cell under investigation was aged by 40 cycles of continuous charge (0.34 A) and discharge (0.68 A) at the elevated temperature of 50 °C; and stored at the shelf for approximately six months at room temperature. Afterwards, the continuous discharge, mixed pulse discharge and driving cycles of NEDC and UDDS were applied to it at 20 °C. The obtained capacity from the mixed pulse discharge test at 20 °C was 1.86 Ah, which results in η_Q being 0.69.

The estimation for the mixed pulse discharge profile, shown in Figure 4c, works well, similarly as for the fresh cell, only with a lower accuracy. The error values are summarized in Table 2. The χ was slightly over estimated at the low voltage plateau with the highest misfit being 0.0550 for $\eta_{Q_{ini}} = 1$ and 0.0461 for $\eta_{Q_{ini}} = 0.69$. This χ over estimation is probably caused in the 'offset' present in the estimated value of the η_Q at the low voltage plateau. In this region, the estimated value in an average was 0.74 for $\eta_{Q_{ini}} = 1$ and 0.71 for $\eta_{Q_{ini}} = 0.69$, while the reference was 0.69. It is also seen that, when the initial value of the η_Q was closer to the reference, the accuracy was again improved.

Table 2. The errors of the state estimation for the aged cell.

Initial Conditions	Average Errors	Maximum Errors
$[\chi = 1\ \eta_Q = 1\ \eta_R = 1]$	[0.0303 0.0633 0.0777]	[0.0550 0.3162 1.4156]
$[\chi = 1\ \eta_Q = 0.69\ \eta_R = 1]$	[0.0274 0.0406 0.0756]	[0.0461 0.1150 1.4155]
NEDC12	[0.0576 0.0974 0.0828]	[0.1123 0.1565 0.5136]
NEDC29	[0.0827 0.1575 0.1796]	[0.1552 0.2412 0.6127]
UDDS12	[0.0797 0.1900 0.1163]	[0.1592 0.3258 0.6686]
UDDS29	[0.0461 0.0696 0.1301]	[0.0890 0.1632 0.6686]

It is important to note that only the model of the fresh cell is implemented in the estimator and it has no knowledge, only assumptions, introduced in Section 3.1, of how the parameters will change with the change of states. In Figure 4a, the actual identified parameters are shown. The low voltage plateau has shrunk more than the high voltage plateau; and therefore the inflection point is moved to the right. Otherwise, the V_{OC} is not changed. However, the R_0 seems to be lower than at the fresh cell, except the very low SOC, where it has increasing tendency.

Besides the mixed pulse discharge profile, four mission driving profiles were also applied to the cell and proceeded to the state estimation. The profiles were: NEDC with the maximum current of 1.2 A (=NEDC12) and of 2.9 A (=NEDC29), and the UDDS also with the maximum currents of 1.2 A (=UDDS12) and of 2.9 A (=UDDS29). The profiles with the estimation results are presented in Figure 6. The χ more or less follows the reference. However, the confidence is reduced and the error can be again related to the estimated η_Q. From the reference η_Q, one can see that it varies from 0.8110 to 1.1965, while the value obtained from the mixed pulse discharge profile was 0.69. The different numbers come from the obtained capacity from the specific tests, which was 1.8592, 2.8221, 2.2029, 3.2499 and 2.4172 Ah for the mixed pulse discharge, NEDC12, NEDC29, UDDS12 and UDDS29, consequently. The actual capacity varies due to its high dependence on the applied current and the dynamics of the profile, which was reported for the Li-S batteries in [38] and investigated and modelled in [39,40]. How it results into the identified parameters is shown in Figure 4d, where the inflection point at V_{OC} and R_0 curves is moving according to the available capacity over the discharge because the SOC is relative to the actual capacity according to (1). Moreover, the dynamics related to the applied current rates and the relaxation periods are visible at the rapidly increasing resistance at the end of discharge. Therefore, the estimated η_Q in our work is related only to the actual profile. If the applied profile remains similar, then the η_Q will straightforwardly indicate the capacity fade ongoing in the cell. In order to have a referent, or so-called independent, actual capacity, which would be related to the capacity fade independent of the mission profile, the dynamics such as transport limitations have to be included in the model.

The estimated η_R seems to have a similar character for all the driving cycles and also the mixed pulse discharge at the aged cell. It is shown in detail in Figure 7. Additionally, the average of the aged cell curves is plotted to highlight the observable trend. At the high voltage plateau, high SOC, the η_R increases sharply and creates a peak around the value of 2. During the flat low voltage plateau in the middle SOC region, there is a smaller increase to around 1.2 and, at the end of discharge (SOC close to 0), there is a decrease down to around 0.6. If this behaviour would be observable over the other cells and mission profiles during aging, it could be also used to couple the resistance change to the capacity fade as it is often done at other battery chemistries.
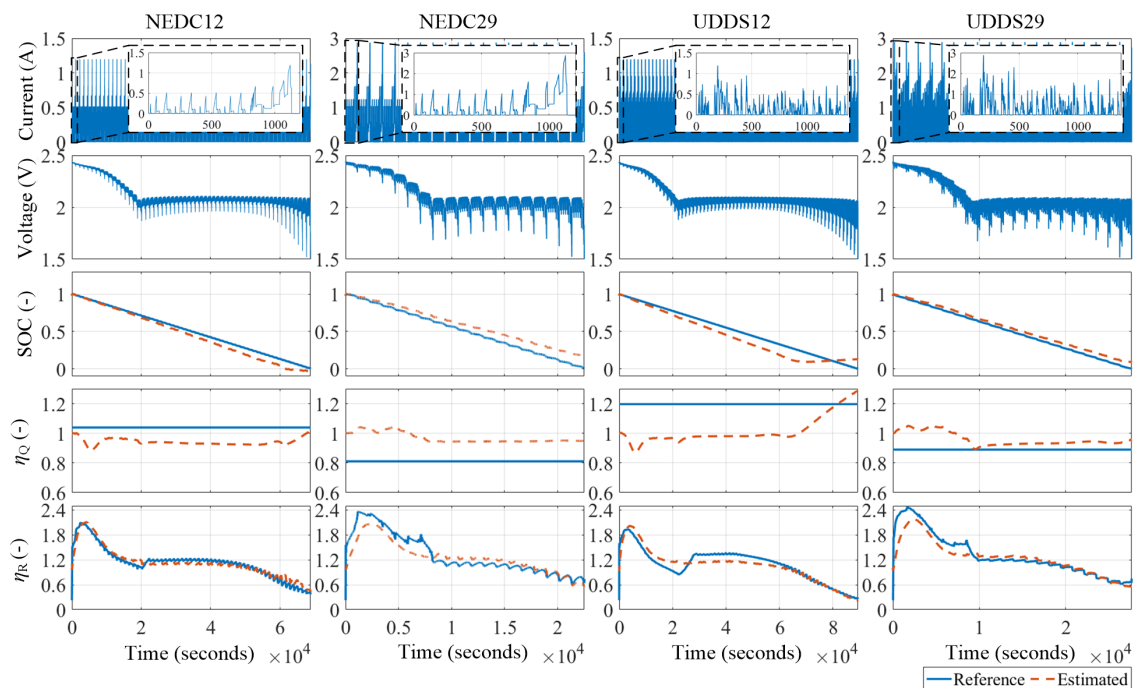
Figure 6. The driving cycle mission profiles and the estimated results for the aged cell. The χ roughly follows the reference. The accuracy of the χ is dependent on the estimated η_Q, which varies with the total discharged capacity of the cell under different mission profiles, due to their different current rates and dynamics. The η_R is in general followed well and is similar between the different driving cycles.
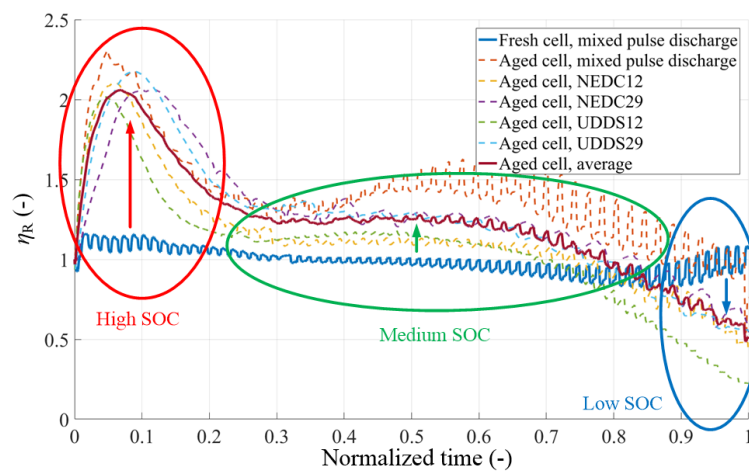

Figure 7. The estimated η_R at the aged cell compared to the fresh cell. The changes in the η_R due to aging are very similar at any mission profile. In the high SOC region, the η_R is rapidly growing. Over the middle SOC region, the η_R slightly grows. Finally, in the low SOC region, the η_R increases.

4.3. Maximum Available Power Estimation Validation

In order to validate the maximum available power estimation, the modified mixed pulse discharge profile was applied to the Li-S cell with considered maximum current pulses and it is shown in Figure 8. After the first set of the discharging pulses with currents of 0.29, 1.45 and 2.90 A, consequently, the discharging pulse with 6.8 A was applied and, after the second set of the discharging pulse, the charging pulse with 1.7 A was applied. When the voltage limits of 1.5 V for discharging and 2.45 V for charging were reached during these maximum current pulses, the operation mode switched from

the constant current mode to constant voltage mode in order to obtain the maximum power in those conditions.
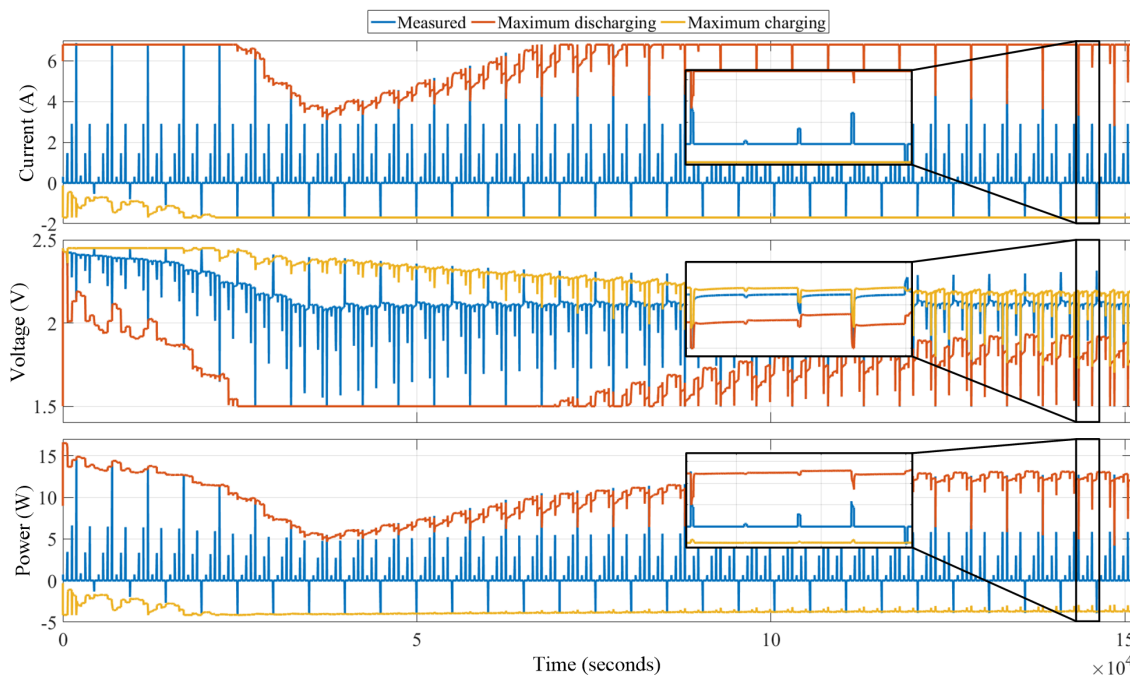

Figure 8. The mixed pulse profile for maximum available power estimation and the instantaneous maximum available power at one second.

We have considered two cases for the power estimation: first, the instantaneous power at $T = 1$ second, shown in Figure 8 and then for the 'accelerating' pulse for $T = 10$ seconds. The accuracy of the estimation is evaluated from the whole 30 second maximum current pulse for the instantaneous power. For the 'accelerating' pulse, only the last 20 seconds of the pulse are considered, as the estimated power is for 10 second application of the maximum current, so the estimated power can be compared just after the first 10 seconds of the applied pulse.

The absolute maximum and average error are computed similarly to equations (65) and (66), consequently, and they are presented in Table 3. Under the selected boundaries of maximum allowed voltage and current limits, the cell was able to provide 14.78 W for discharge and 4.14 W for charge during the applied pulses. The absolute maximum errors seem to reach high significant values related to the maximum cell performance. However, the absolute average errors are fairly acceptable. It is also important to keep in mind that the model was derived and accounted for maximum discharging current 2.9 A and no charging model or parameters are implemented. Therefore, the performance of the maximum available power estimator, while applying current of 6.8 A for discharge, which is more than two times that for the model that was parametrized, and 1.7 A charging current, is considered as more than acceptable.

Table 3. The errors of maximum available power estimation.

T	Quantity	Average Errors	Maximum Errors
1 s	$[V_{min}\ V_{max}]$ (V)	[0.0080 0.0460]	[0.1840 0.1556]
	$[I_{P_{dis.max}}\ I_{P_{ch.max}}]$ (A)	[0.3022 0.0249]	[1.7750 0.7759]
	$[P_{dis.max}\ P_{ch.max}]$ (W)	[0.5049 0.1381]	[3.0365 1.9128]
10 s	$[V_{min}\ V_{max}]$ (V)	[0.0110 0.0525]	[0.2148 0.1548]
	$[I_{P_{dis.max}}\ I_{P_{ch.max}}]$ (A)	[0.6119 0.0284]	[3.6860 0.3566]
	$[P_{dis.max}\ P_{ch.max}]$ (W)	[0.9924 0.1586]	[6.1106 0.8736]

5. Conclusions

In this work, a novel SOC and SOH estimation method for Li-S batteries has been introduced, together with a specifically tailored model for maximum available power estimation. The proposed estimation algorithm is based on two extended Kalman filters, where the first filter is used for online parameter identification of the battery electrical circuit model using voltage and current measurements. Subsequently, the estimated battery parameters are used in the second extended Kalman filter to estimate the SOC, the SOH, (in terms of both capacity fade and the resistance change) and the maximum available power for both charging and discharging pulses.

The robustness and the accuracy of the proposed SOC and SOH estimator has been analyzed using a mixed pulse discharge profile firstly for a fresh cell and then for an aged cell. The estimator does not include any process model of the Li-S battery degradation and it is solely based on the error correction. The estimator has shown the capability to track the SOC, the capacity fade and the resistance change for an aged cell with the worst case average errors being 0.0827, 0.1900 and 0.1796, respectively. However, the accuracy of the SOC is dependent on the estimated capacity fade, which varies depending on the current rates and dynamics of the considered mission profiles. Therefore, there is a need for the concept clarification of the actual capacity at the Li-S batteries according to their dynamics and history. Moreover, the model for the available capacity change would be helpful in order to provide information about the absolute capacity fade. In terms of the absolute capacity fade, the resistance change could be used as a supportive indicator, as it has shown a more consistent trend between the fresh and the aged cell. However, the question of how it evolves under different degradation conditions has to be still answered.

The implemented maximum available power estimator was presented and validated by comparing the obtained estimation results with the experimental tests. The proposed model proofed to be robust also when currents of 6.8 A were applied, which is more than two times the value of the current, which had been used for the model parametrization. Furthermore, the available power estimation algorithm provides relatively accurate results for the case when the available power should be predicted during battery charging, a case that was not considered either during the parametrization stage.

Abbreviations

The following abbreviations and symbols are used in this manuscript:

ANFIS	Adaptive Neuro-Fuzzy Inference System
BMS	Battery Management System
EKF	Extended Kalman filter
Li-ion	Lithium-Ion
Li-S	Lithium-Sulfur
NEDC	New European Driving Cycle
NiMH	Nickel-Metal hydride

OCV	Open-Circuit Voltage
OEMs	Original Equipment Manufacturers
RSME	Root Square Mean Error
SOC	State of Charge
SOH	State of Health
UDDS	Urban Dynamometer Driving Schedule

Battery States and Model's Parameters and Variables:

χ	SOC
$Q_{present}$	a present amount of charge in the battery, which is possible to extract
$\bar{Q}_{cap}$	the initial capacity; the maximum extractable charge from the fully charged battery at the beginning of life
Q_{cap}	the actual capacity; the maximum extractable charge from the fully charged battery at the actual battery age
η_{Q}	the capacity fade
η_{R}	the internal resistance change
$\bar{R}_0$	the initial internal resistance at the beginning of life
R_0	the actual internal resistance at the beginning of life
$P_{dis.max}$	the maximum available discharging power
$P_{ch.max}$	the maximum available charging power
P_{max}	the maximum available power (a generalized term)
V_{OC}	the open-circuit voltage
R_1	the resistor in the *RC* element
C_1	the capacitor in the *RC* element
V_p	the voltage over the *RC* element
I_L	the load current
V_L	the battery terminal voltage
$\gamma_{m,c}$	the term for the transition point between the high and the low voltage plateaus
m	a scaling factor for the maximal gradient of the sinusoidal function
c	the transition point, both functions are equally represented there
Ω	the dynamic bandwidth
R_{int}	the total steady-state resistance
ρ	the dynamic fraction of the response

Extended Kalman Filter:

A	state matrix
B	input matrix
C	output matrix
D	feedthrough matrix
x	model's states
y	model's outputs
u	model's inputs
k	the discrete time index
h	the nonlinear measurement function
P	the error covariance matrix
Q	the process noise covariance matrix
R	the noise measurement covariance matrix
K	the Kalman gain matrix
v	the measurement noise vector
w	the process noise vector
W_0	the 'observability grammian'
$x_{\_MaxErr}$	the absolute maximum error
$x_{\_AvgErr}$	the absolute mean error

References

1. Bruce, P.G.; Freunberger, S.A.; Hardwick, L.J.; Tarascon, J.M. Li-O$_2$ and Li-S batteries with high energy storage. *Nat. Mater.* **2012**, *11*, 19–29, doi:10.1038/nmat3191. [CrossRef] [PubMed]
2. Hunt, I.A.; Patel, Y.; Szczygielski, M.; Kabacik, L.; Offer, G.J. Lithium sulfur battery nail penetration test under load. *J. Energy Storage* **2015**, *2*, 25–29, doi:10.1016/j.est.2015.05.007. [CrossRef]

3. Risse, S.; Cañas, N.A.; Wagner, N.; Härk, E.; Ballauff, M.; Friedrich, K.A. Correlation of capacity fading processes and electrochemical impedance spectra in lithium/sulfur cells. *J. Power Source* **2016**, *323*, 107–114, doi:10.1016/j.jpowsour.2016.05.032. [CrossRef]

4. Knap, V.; Stroe, D.I.; Swierczynski, M.; Teodorescu, R.; Schaltz, E. Investigation of the Self-Discharge Behavior of Lithium-Sulfur Batteries. *J. Electrochem. Soc.* **2016**, *163*, A911–A916, doi:10.1149/2.0641606jes. [CrossRef]

5. Xu, W.T.; Peng, H.J.; Huang, J.Q.; Zhao, C.Z.; Cheng, X.B.; Zhang, Q. Towards Stable Lithium-Sulfur Batteries with a Low Self-Discharge Rate: Ion Diffusion Modulation and Anode Protection. *ChemSusChem* **2015**, *8*, 2892–2901, doi:10.1002/cssc.201500428. [CrossRef] [PubMed]

6. Wild, M.; O'Neill, L.; Zhang, T.; Purkayastha, R.; Minton, G.; Marinescu, M.; Offer, G.J. Lithium Sulfur Batteries, A Mechanistic Review. *Energy Environ. Sci.* **2015**, *8*, 3477–3494, doi:10.1039/C5EE01388G. [CrossRef]

7. Waag, W.; Fleischer, C.; Sauer, D.U. Critical review of the methods for monitoring of lithium-ion batteries in electric and hybrid vehicles. *J. Power Source* **2014**, *258*, 321–339, doi:10.1016/j.jpowsour.2014.02.064. [CrossRef]

8. Meng, J.; Ricco, M.; Luo, G.; Swierczynski, M.; Stroe, D.I.; Stroe, A.I.; Teodorescu, R. An Overview and Comparison of Online Implementable SOC Estimation Methods for Lithium-Ion Battery. *IEEE Trans. Ind. Appl.* **2018**, *54*, 1583–1591, doi:10.1109/TIA.2017.2775179. [CrossRef]

9. Shahriari, M.; Farrokhi, M. Online State-of-Health Estimation of VRLA Batteries Using State of Charge. *IEEE Trans. Ind. Electron.* **2013**, *60*, 191–202, doi:10.1109/TIE.2012.2186771. [CrossRef]

10. Bhangu, B.S.; Bentley, P.; Stone, D.A.; Bingham, C.M. Nonlinear observers for predicting state-of-charge and state of health of lead-acid batteries for hybrid-electric vehicles. *IEEE Trans. Veh. Technol.* **2005**, *54*, 783–794, doi:10.1109/TVT.2004.842461. [CrossRef]

11. Coleman, M.; Lee, C.K.; Zhu, C.; Hurley, W.G. State-of-Charge Determination From EMF Voltage Estimation: Using Impedance, Terminal Voltage, and Current for Lead-Acid and Lithium-Ion Batteries. *IEEE Trans. Ind. Electron.* **2007**, *54*, 2550–2557, doi:10.1109/TIE.2007.899926. [CrossRef]

12. Galeotti, M.; Giammanco, C.; Cinà, L.; Cordiner, S.; Carlo, A.D. Synthetic methods for the evaluation of the State of Health (SOH) of nickel-metal hydride (NiMH) batteries. *Energy Convers. Manag.* **2015**, *92*, 1–9, doi:10.1016/j.enconman.2014.12.040. [CrossRef]

13. Singh, P.; Fennie, C., Jr.; Reisner, D. Fuzzy logic modelling of state-of-charge and available capacity of nickel/metal hydride batteries. *J. Power Source* **2004**, *136*, 322–333, doi:10.1016/j.jpowsour.2004.03.035. [CrossRef]

14. Fotouhi, A.; Propp, K.; Auger, D.J. Electric vehicle battery model identification and state of charge estimation in real world driving cycles. In Proceedings of the 2015 7th Computer Science and Electronic Engineering Conference (CEEC), Colchester, UK, 24–25 September 2015, doi:10.1109/CEEC.2015.7332732. [CrossRef]

15. Plett, G.L. Extended Kalman filtering for battery management systems of LiPB-based {HEV} battery packs: Part 3. State and parameter estimation. *J. Power Source* **2004**, *134*, 277–292, doi:10.1016/j.jpowsour.2004.02.033. [CrossRef]

16. Charkhgard, M.; Farrokhi, M. State-of-Charge Estimation for Lithium-Ion Batteries Using Neural Networks and EKF. *IEEE Trans. Ind. Electron.* **2010**, *57*, 4178–4187, doi:10.1109/TIE.2010.2043035. [CrossRef]

17. Mikhaylik, Y.V.; Akridge, J.R. Polysulfide Shuttle Study in the Li/S Battery System. *J. Electrochem. Soc.* **2004**, *151*, A1969, doi:10.1149/1.1806394. [CrossRef]

18. Fotouhi, A.; Auger, D.; Propp, K.; Longo, S. Electric Vehicle Battery Parameter Identification and SOC Observability Analysis: NiMH and Li-S Case Studies. In Proceedings of the 8th IET International Conference on Power Electronics, Machines and Drives (PEMD 2016), Glasgow, UK, 19–21 April 2016, doi:10.1049/cp.2016.0142. [CrossRef]

19. Propp, K.; Auger, D.J.; Fotouhi, A.; Longo, S.; Knap, V. Kalman-variant estimators for state of charge in lithium-sulfur batteries. *J. Power Source* **2017**, *343*, 254–267, doi:10.1016/j.jpowsour.2016.12.087. [CrossRef]

20. Propp, K.; Marinescu, M.; Auger, D.J.; O'Neill, L.; Fotouhi, A.; Somasundaram, K.; Offer, G.J.; Minton, G.; Longo, S.; Wild, M.; et al. Multi-temperature state-dependent equivalent circuit discharge model for lithium-sulfur batteries. *J. Power Source* **2016**, *328*, 289–299, doi:10.1016/j.jpowsour.2016.07.090. [CrossRef]

21. Fotouhi, A.; Auger, D.J.; Propp, K.; Longo, S. Accuracy Versus Simplicity in Online Battery Model Identification. *IEEE Trans. Syst. Man Cybern. Syst.* **2016**, *PP*, 1–12, doi:10.1109/TSMC.2016.2599281. [CrossRef]

22. Propp, K.; Auger, D.J.; Fotouhi, A.; Marinescu, M.; Knap, V.; Longo, S. Improved State of Charge Estimation for Lithium-Sulfur Batteries. Available online: https://doi.org/10.17862/cranfield.rd.c.3723934 (accessed on 14 August 2018).

23. Bohlen, O.; Gerschler, J.B.; Sauer, D.U.; Keller, M. Robust Algorithms for a Reliable Battery Diagnosis—Managing Batteries in Hybrid Electric Vehicles. In Proceedings of the 22nd International Battery, Hybrid and Fuel Cell Electric Vehicle Symposium and Exposition, Yokohama, Japan, 23–28 October 2006.

24. Waag, W.; Fleischer, C.; Sauer, D.U. Adaptive on-line prediction of the available power of lithium-ion batteries. *J. Power Source* **2013**, *242*, 548–559, doi:10.1016/j.jpowsour.2013.05.111. [CrossRef]

25. Fleischer, C.; Waag, W.; Bai, Z.; Sauer, D.U. On-line self-learning time forward voltage prognosis for lithium-ion batteries using adaptive neuro-fuzzy inference system. *J. Power Source* **2013**, *243*, 728–749, doi:10.1016/j.jpowsour.2013.05.114. [CrossRef]

26. Farmann, A.; Waag, W.; Marongiu, A.; Sauer, D.U. Critical review of on-board capacity estimation techniques for lithium-ion batteries in electric and hybrid electric vehicles. *J. Power Source* **2015**, *281*, 114–130, doi:10.1016/j.jpowsour.2015.01.129. [CrossRef]

27. Balagopal, B.; Chow, M.Y. The state of the art approaches to estimate the state of health (SOH) and state of function (SOF) of lithium Ion batteries. In proceedings of the 2015 IEEE 13th International Conference on Industrial Informatics (INDIN), Cambridge, UK, 22–24 July 2015, doi:10.1109/INDIN.2015.7281923. [CrossRef]

28. Peukert, W. Über die Abhängigkeit der Kapazität von der Entladestromstärke bei Bleiakkumulatoren. *Elektrotech. Z.* **1897**, *20*, 20–21.

29. Hausmann, A.; Depcik, C. Expanding the Peukert equation for battery capacity modeling through inclusion of a temperature dependency. *J. Power Source* **2013**, *235*, 148–158, doi:10.1016/j.jpowsour.2013.01.174. [CrossRef]

30. Galeotti, M.; Cina, L.; Giammanco, C.; Cordiner, S.; Carlo, A.D. Performance analysis and SOH (state of health) evaluation of lithium polymer batteries through electrochemical impedance spectroscopy. *Energy* **2015**, *89*, 678–686, doi:10.1016/j.energy.2015.05.148. [CrossRef]

31. Schmidt, A.P.; Bitzer, M.; Imre, Á.W.; Guzzella, L. Model-based distinction and quantification of capacity loss and rate capability fade in Li-ion batteries. *J. Power Source* **2010**, *195*, 7634–7638, doi:10.1016/j.jpowsour.2010.06.011. [CrossRef]

32. Richter, G. Method and Device for Determining the State of Function of an Energy Storage Battery. US Patent 6,885,951, 26 April 2005.

33. Understanding Nonlinear Kalman Filters, Part II: An Implementation Guide. Available online: http://www2.statler.wvu.edu/ irl/page13.html (accessed on 9 August 2018).

34. Welch, G.; Bishop, G. An Introduction to the Kalman Filter. In Proceedings of the SIGGRAPH, Chapel Hill, NC, USA, 24 July 2006.

35. Chiang, Y.H.; Sean, W.Y.; Ke, J.C. Online estimation of internal resistance and open-circuit voltage of lithium-ion batteries in electric vehicles. *J. Power Source* **2011**, *196*, 3921–3932. [CrossRef]

36. He, H.; Xiong, R.; Guo, H. Online estimation of model parameters and state-of-charge of LiFePO$_4$ batteries in electric vehicles. *Appl. Energy* **2012**, *89*, 413–420. [CrossRef]

37. Xiong, R.; He, H.; Sun, F.; Zhao, K. Evaluation on state of charge estimation of batteries with adaptive extended Kalman filter by experiment approach. *IEEE Trans. Veh. Technol.* **2013**, *62*, 108–117. [CrossRef]

38. Knap, V.; Zhang, T.; Stroe, D.I.; Schaltz, E.; Teodorescu, R.; Propp, K. Significance of the Capacity Recovery Effect in Pouch Lithium-Sulfur Battery Cells. *ECS Trans.* **2016**, *74*, 95–100, doi:10.1149/07401.0095ecst. [CrossRef]

39. Zhang, T.; Marinescu, M.; Walus, S.; Offer, G.J. Modelling transport-limited discharge capacity of lithium-sulfur cells. *Electrochim. Acta* **2016**, *219*, 502–508, doi:10.1016/j.electacta.2016.10.032. [CrossRef]

40. Zhang, T.; Marinescu, M.; Walus, S.; Kovacik, P.; Offer, G.J. What Limits the Rate Capability of Li-S Batteries during Discharge: Charge Transfer or Mass Transfer? *J. Electrochem. Soc.* **2018**, *165*, A6001–A6004, doi:10.1149/2.0011801jes. [CrossRef]